Cleaner Engineering and Technology 3 (2021) 100108

Contents lists available at ScienceDirect

Cleaner Engineering and Technology

journal homepage: www.sciencedirect.com/journal/cleaner-engineering-and-technology

Synthesis and characterization of aluminium oxide nanoparticles from waste aluminium foil and potential application in aluminium-ion cell

Mercy Njeri Nduni [a], Aloys Mosima Osano [b], Bakari Chaka [a,*]

[a] Department of Mathematics and Physical Sciences, Maasai Mara University, Kenya. P.O Box 861-20500, Narok, Kenya
[b] Centre for Innovation, New and Renewable Energy, Maasai Mara University, Kenya. P.O Box 861-20500, Narok, Kenya

ARTICLE INFO

Keywords:
Aluminium wastes
Al_2O_3 nanoparticles
Aluminium-ion cell

ABSTRACT

Aluminium waste accumulated in landfills is a solid waste in abundance. Various methods have been employed to alleviate the waste only to yield secondary pollution effects. This study seeks to provide an alternative greener recycling procedure that is beneficial to society in terms of health and economics through energy storage materials. The study aimed to synthesize and characterize aluminium oxide nanoparticles from waste aluminium foil and its potential applications in fabricating aluminium-ion cell, FAIC.[1] Aluminium oxide nanoparticles were obtained by co-precipitation of waste aluminium foils at constant annealing room temperature followed by mechanical milling to nanoparticulate range. The particles were then characterized for particle size and phases (X-ray diffraction), functional groups and optical activity (infra-red and ultra-violet-visible spectroscopy respectively). Cell assembling of FAIC was done using a graphite anode while the cathode had a standard and the synthesized aluminium oxide nanoparticles. Sulfuric acid and magnesium sulfate electrolytes were used with two binders; polyacrylate and silicone adhesives. The average synthesis yield was 40.64 $\pm$ 19.69%. Most of the particles had a α-Al_2O_3 and γ-Al_2O_3 phase with an average size of 63.763 nm and 66.5144 nm for the two polymorphs respectively. There were several OH-groups coupled to Al–O bonds. The optimal absorption peak was λ_{max} = 237 nm corresponding to a band gap of 5.25eV. The synthesized nanoparticles exhibited great electrochemical potential, nearing the standard one in most of the parameters. The FAIC potential, current, power densities and polarization curves from sulfuric acid electrolyte and polyacrylate binder were significantly higher to those of magnesium sulfate and silicone binder ($P > 0.05$).

1. Background of study

Aluminium foils are widely used as food wraps and in other functions in the homes and in restaurants. Their wastes end up in landfills. There are various methods that have been employed to eliminate aluminium waste from the environment. The most common method is recycling aluminium waste (Yusuf et al., 2019). However, the current methods used have a lot of limitations and end up causing more pollution. This is because recycling requires heavy machines that are used to shred, melt and compress the aluminium. Some of these processes are powered by burning fossil fuels such as coal which is a great emitter of oxides of nitrogen and sulfur leading to air pollution (Li et al., 2017). Additionally, when aluminium is melted it causes health problems including: liver damage, skin disorder, certain types of cancer and immune system impairment (Klotz et al., 2017). This justifies the need for greener recycling methods. The better alternative chosen here is its applications in the form of nanoparticles in rechargeable aluminium ion cells, AICs.

Nanoparticles are particles between 1 and 100 nm in size with a surrounding interfacial layer (Hoshyar et al., 2016). The main advantage of using nanoparticles in batteries are; greater surface area of the electrode, reduced flammability of electrode material (Roselin et al., 2019), increased power output, decreased recharge time and increased battery shelf life (Oh et al., 2013). Lin et al. (2015) came up with an ultrafast rechargeable aluminium ion battery which consisted aluminium metal as the anode and graphite foam as the cathode. The battery could undergo up-to 7500 charge cycles without discharge

Abbreviations: AIC, Aluminium ion cell; PVDF, Polyvinylidene fluoride; SA, Silicone adhesive; PA, Polyacrylate adhesive; OCV, Open current voltage; CCV, Closed current voltage.

* Corresponding author.
E-mail addresses: nduni036@student.mmarau.ac.ke (M.N. Nduni), aloysosano@mmarau.ac.ke (A.M. Osano), bakarichaka@mmarau.ac.ke (B. Chaka).

[1] Aluminium-ion cell.

https://doi.org/10.1016/j.clet.2021.100108
Received 3 August 2020; Received in revised form 23 March 2021; Accepted 12 May 2021
Available online 17 May 2021

capacity decay (Lin et al., 2015). Nanoparticle technology has been used to increase battery performance by changing the internal resistance of batteries (Mahmood and Hou, 2014). Nanotechnology can increase the side and surface area of the electrodes and batteries. This is done by making electrodes sponge-like thus making them able to absorb more energy during charging process. This process increasing the energy storage capacity. Wang et al. (2017) showed that aqueous electrolytes show several advantages regarding low cost, simple operation and environmental friendliness over non-aqueous electrolytes. The advantages of resource abundance and low cost promote alternative batteries, as one of promising alternatives to the state-of-art Lithium-ion batteries.

Use of sulfate-based electrolytes is common and quite effective due to the high dissociation of the ions at a wider scope of electrochemical environment (Leustek, 2002), (Badwal et al., 2014). Magnesium sulfate and sulfuric acid have continuously been used as electrolytes in several galvanic and electrochemical cells (Badwal et al., 2014). Several lithium-ion (Li-ion) batteries use these two electrolytes. Graphite electrodes also enjoy a high working efficiency with numerous transition metal and transition metal-like oxides (Yin et al., 2018), such as those of aluminium. Both silicone and polyacrylate are taunted as potential substitutes for traditional electrode binders such as polyvinylidene fluoride (PVDF[2]), polyamide imide, polyethylene glycol, polyvinyl alcohol and many others. The two binders have excellent adhesion, cohesion and wettability properties necessary for binding electrodes (Toigo et al., 2020). They can also perform optimally in a wide range of chemical, mechanical, thermal and electrochemical environment (Toigo et al., 2020).

In this study, the accumulated and environmentally pollutant waste aluminium foil in landfills were recycled by converting them to nanoparticles and using the nanoparticles in fabricating environmentally and cost friendly AICs. This process is green since it will reduce the energy required to manufacture products reducing gaseous emissions. The current study was geared to synthesize and characterize aluminium oxide nanoparticles from aluminium waste and potential applications in the fabrication of AICs. There are abundant waste aluminum foils and conventional methods used to recycle them generate secondary pollution. Their utilization in energy storage devices is thus a greener option aimed at reducing pollution while generating energy. There is a justifiable need for alumina nanoparticles due to their numerous applications. Inefficiencies in microparticulate AICs (such as energy losses) further necessitate the production of nanoparticulate alumina electrodes.

2. Materials and methods

2.1. Experimental design

Sampling was carried out around Maasai Mara University, Narok town, Kenya. This region is densely populated with landfills and aluminium wastes form a great part of these landfills. The town has the coordinates 35.8771°E, 1.0875°S. It is located west of Nairobi, southwest of the country along the Great Rift Valley. The samples collected were 50 waste aluminium foils. Samples were only collected once without any further replicates. Samples were collected by a completely randomized design. This minimized biasness in the experimental samples chosen enabling all types of aluminium wastes to be used for electricity generation. All analysis except UV-VIS and XRD analysis (which were carried out from Vaal University of Technology, South Africa) were done from the Chemistry lab. Maasai mara university, Kenya.

Aluminium oxide nanoparticles were obtained from waste aluminium foils and hydrochloric acid and two salts (sodium chloride and sodium carbonate) while drying at constant temperature. Thorough washing was done on the residue which was then oven-dried before reducing the particle size to nanoparticle range. Thereafter, the particles were characterized for functional groups (FT-IR), absorption bands (UV-VIS), crystallinity, phase and size determination (XRD). The particles were then used to develop suitable working electrodes (with different conductive binders being used). The electrodes were then used to assemble an aluminium ion-cell with two electrolyte solutions being used ($MgSO_4$ and H_2SO_4). The electrochemical characterizations of the various combinations of both the synthesized and standard Al_2O_3 were determined using a multi-meter.

2.2. Methods

2.2.1. Sample preparation

Aluminium waste samples were thoroughly cleaned using water to remove any accumulated debris on the surface. The samples were then dried in an oven for 4 h. Sample pretreatment was done by gradually filing the surface to remove oxide layers.

2.2.2. Synthesis of white aluminium oxide nanoparticles

56.6 ml of HCl acid (36% $^{v}/_{v}$) and an equal amount of water were mixed at −10 °C. Approximately 40.0g of waste aluminium foil was then gradually added into the reactor until effervescence stopped (equation (1)).

$$HCl_{(aq)} + Al_{(s)} \rightarrow Al_2Cl_{6(aq)} + H_{2(g)} \quad (1)$$

The solution was then filtered to remove impurities and cooled. A concentration of 1M sodium carbonate was slowly added to precipitate the aluminium oxide in the filtrate formed ensuring all aluminium chloride had been converted to aluminium oxide (equation (2)).

$$Al_2Cl_{6(aq)} + 3Na_2CO_{3(aq)} \rightarrow 3CO_{2(g)} + Al_2O_{3(s)} + 6NaCl_{(aq)} \quad (2)$$

More distilled water was added to aluminium oxide and it was left to settle for 1 h. The clear liquid solution was decanted and then more water was added. It was left to settle before it was decanted again (to wash off the sodium chloride). The solution was then filtered to obtain aluminium oxide, which was then dried in an oven at 100 °C for 3–4 h to remove water. Mechanical milling was applied to reduce the particles to nanoparticle scale. In this case, the residue was crushed into fine powder and sieved using different pore-sized sieves.

2.2.3. Characterization of synthesized Al_2O_3 nanoparticles

Absorption bands of the synthesized particles were determined by a blank scan using UV-VIS (Shimadzu-1800) spectroscopy. Color development was done using n-hexane solution which was used as the blank. The samples were prepared and the absorbance measured between 280 and 400 nm wavelength. The functional groups of the particles were confirmed by FT-IR (Shimadzu-119) spectroscopy. About 10 mg of the dried powder was mixed with 200 mg KBr crystals and further crushed for homogenization. The mixture was then put in sample compartment and FT-IR Spectra monitored. Crystallinity, size and phase analysis was done using X-Ray Diffractometer-7000 (Shimadzu). The samples in form of milled powder were placed on steel sample holders and leveled to obtain total and uniform X-ray exposure. The samples were then analyzed at room temperature (25 °C) with a monochromatic CuKα radiation source (λ = 0.1539 nm) in the step-scan mode with a 2θ angle ranging from 10° to 80° with a step of 0.04 and scanning time of 5.0 min. Particle size was determined by the Scherrer formula (equation (3));

$$D = \frac{K\lambda}{\beta Cos\theta} \quad (3)$$

Where D is the crystal size (nm), λ is the wavelength of the X-ray beam, K is the constant (0.94), β is the peak width at half maximum intensity and θ is the peak position used to derive the crystallite size.

[2] Polyvinylidene fluoride.

2.2.4. Electrode preparations and assembly of fabricated aluminium ion cell, AIC

An aluminium ion-cell was fabricated for the corresponding amperiometric and voltametric analyses. Graphite rod (SFG6L) was used to make the anode while the cathode was varied between standard and the synthesized Al_2O_3 nanoparticles. Two commercial conductive binders i. e Silicone adhesive (SA[3]) and Polyacrylate Adhesive (PA[4]) were used to enjoin the particles onto the supporting rod (graphite) in the ratio of 90:10. Graphite was preferred for its ability to improve the reversible charge density and electrode adhesion for favorable industrial processability. The electrode suspensions were gradually kneaded for around 20 min between 20 and 30 °C and stirred at 400–500 rpm. The suspension was then left overnight under room pressure and cast on aluminum foil (Korff AG, Switzerland) with a thickness of 22 μm as a current collector to yield the electrode. The electrodes were manually calendared with little pressure and molded in the desired shapes to obtain workable compact electrodes. The aeral mass loading was 20mgcm^{-3}. An electrode length of 57±2 mm, external diameter 6 ± 0.5 mm and electrode composite density of 3.6gcm^{-3} was arrived at.

The aluminium ion-cell was fabricated using a cuboid polymeric insulator (dimensions 130 mm by 220 mm base area and height 100 mm). The electrolytes used were 1.0M magnesium sulfate and sulfuric acid.

2.2.5. Electrochemical tests

All the voltage readings were recorded using a multi-meter (Model: UT33B; DC Voltage: 200 mV, 2000 mV, 20V, 200V±(0.5% + 2)/500V± (0.8% + 2); AC Voltage: 200V/500V±(1.2% + 10) and DC Current (A)) at room temperature and pressure. The resistance of the multi-meter during the closed-circuit voltage experiments was 100Ω. The performance of the synthetic aluminium oxide nanoparticles were compared with those of standard aluminium oxide nanoparticles (Catalog Number, ACM11092323-61; CAS 11092-32-3). The procedure was then repeated using different electrolytes, cathodes and conductive electrode binders. A graphite anode of similar volume to the cathode one (1107 ± 176 mm^3) was constantly used for all the experiments while the cathode one was varied. For the polarization studies, graphite rod (SFG6L) was used as the reference electrode.

2.3. Data analysis

Data analysis of the various statistics computations was done using Ms. Excel (version 2016) and Originlab (version 6.5). A confidence level of 95% (P) and 3 degrees of freedom was used. The average data were presented as mean ± standard deviation.

3. Results and discussions

3.1. Synthesis of aluminium oxide particles

Aluminium oxide particles obtained were white in color. The particles had a weight of 74.34g which were then crushed to yield a weight of 52.36g. This reduction in weight is due to the continuous grinding and it yielded the aluminium oxide particles. The percentage yield of the aluminium oxide particles was 40.64 ± 19.69%.

3.2. Characterization of Al_2O_3 nanoparticles

3.2.1. Functional group analysis

The IR spectra of the synthesized and standard aluminium oxide particles resembled towards the blue end with several peaks being cited in both samples. The synthesized aluminium oxide particles had more samples at the fingerprint region owing to impurities resulting from the waste aluminium samples used. Both samples exhibited presence of moisture as seen in the peaks between 3600 and 4000 cm^{-1}. The synthesized particles exhibited presence of alkanols (3300 cm^{-1}). These compounds also resulted due to presence of organic contaminants in the waste used to prepare the particles. More organic compounds were depicted by presence of hydrogenic sp, sp^2 and sp^3 peaks (at 3,572 cm^{-1}, 3,467 cm^{-1} and 2,924 cm^{-1} respectively). O–H stretching of α-Al_2O_3 nanoparticles have also been exhibited at 3,457 cm^{-1} and 3,438 cm^{-1} (Ates et al., 2015) as was the case in the synthesized spectra (Fig. 1b). The latter peak was also observed in the standard aluminium oxide sample. The standard aluminium oxide sample however had a rather plateau-like spectra, devoid of major peaks between 2250 and 1,250 cm^{-1}. This was largely contrasted with that of the synthesized nanoparticles which had several peaks in that range due to impurities and reagents used during preparation. Some of these peaks include the cis-double bond at 1,566 cm^{-1} and benzylic double bond at 1,388 cm^{-1}. Al–O stretching peaks have previously been observed at 459, 595, and 656 cm^{-1} (for octahedral structures) while bands around 715 cm^{-1} and 1072 cm^{-1} are related to Al–O stretching mode in tetrahedron and symmetric bending of Al–O–H, respectively (Djebaili et al., 2015). Both the standard and synthesized particles spectra had these characteristic peaks, affirming presence of Al–O. Fig. 1 illustrates these two spectra.

3.2.2. X-ray diffraction analysis

Data obtained from the diffractogram were matched with the database of the Joint Committee on Powder Diffraction Standards (JCPDS) card file No. 46–1215, which confirmed the crystalline structure of Al_2O_3 nanoparticles. There are 4 main polymorphs associated with alumina nanoparticles i.e. α, θ, γ and κ. Polymorphic phase change is associated with change in crucial lattice parameters such as particle diameter and density. The Al_2O_3 samples analyzed showed presence of α and γ aluminium oxide nanoparticle crystal phases and some traces of elemental aluminium. The α-Al_2O_3 polymorphs were observed for the larger peaks of the sample i.e. at 31.96° and 56.62°. These phases are known to exist at lower temperature conditions (Mikhaylo et al., 2005), (Umemoto and Wentzcovitch, 2008). γ-Al_2O_3 phase occur at higher temperature regimes and was observed at 45.66°. Annealing of Al_2O_3 by gradual oxidation lead to growth of the otherwise naturally amorphous layer of Al_2O_3 (Wang et al., 2015). The kinetics of the reactions are governed by outward diffusion of alumina ions (Wang et al., 2016). In the process, a critical thickness layer is formed which differentiate the α-Al_2O_3 from the γ-Al_2O_3 phases. The latter phase is therefore larger due to the growth of the polymorph and the critical layer (≈5 nm). Further growth of the polymorph lead to formation of θ-Al_2O_3 (Ates et al., 2015). The α-Al_2O_3 polymorphs are the smallest, most stable and dense (Vailionis et al., 2011). This phase is attained after continuous oxidation of the θ-Al_2O_3 which is accompanied by inner grain boundary diffusion of oxygen anions (Bagwell et al., 2001). This inward shift is responsible for the relatively more compact α-Al_2O_3. The indices of the major peaks in the diffractogram were matched as following; 2θ angle 27.66° (012), 31.96° (104), 45.68° (113), 54.04° (024), 56.62° (116) and 66.4° (214). The largest peak was observed at angle 2θ = 31.96° with an intensity of 2470 counts. The peak corresponded to α-Al_2O_3 as well as boehmite crystal structures with octahedral and orthorhombic dipyramidal shapes (Santos et al., 2009), (Iijima et al., 2016). Co-occurrence of α-Al_2O_3 and boehmite structures revealed that the compound was not pure. This could be attributed to the source of the alumina. This structure has desirable characteristics suitable as a battery electrode such as good water release patterns, slow polymerization and condensation pathways (Krewski et al., 2007). Most boehmite structures are optically active with a specific gravity of 3.00–3.07 g/ml (Conroy et al., 2017). The calculated size of this structure (using Scherrer equation) was 63.763 nm. The other large peak was observed at angle 2θ = 45.68°. This peak corresponded to rhombohedral crystal structure (lattice parameters a = 4.76 Å and b = 12.99 Å). This structure also has desirable thermoelectric

[3] Silicone adhesive.
[4] Polyacrylate adhesive.

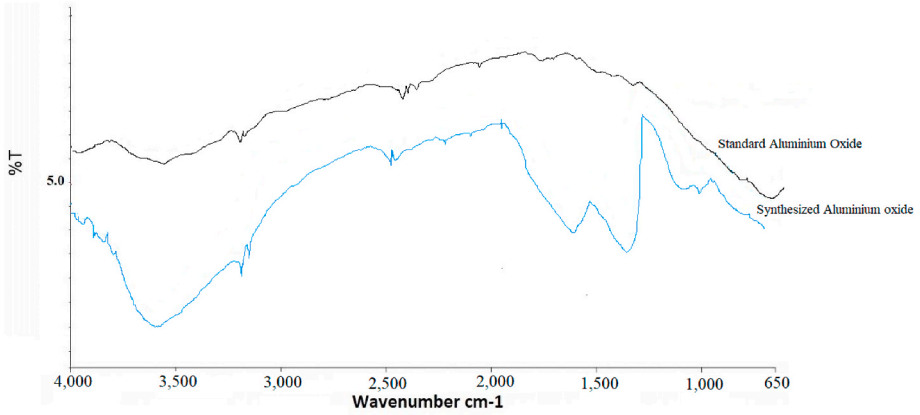

Fig. 1. FT-IR spectra of standard and synthesized aluminium oxide nanoparticles.

and anisotropic behavior as a cell electrode. The calculated diameter of particles with this structure in the samples (using Scherrer formula) was 66.5144 nm. The diffractogram of the synthesized alumina particles is illustrated in Fig. 2.

3.2.3. UV-VIS analysis

The UV-VIS spectrum was used to understand the electronic structure of the optical band gap of the samples. Absorption in the near ultraviolet region arises from electronic transitions associated within the sample (Prasad et al., 2017). In comparison with UV–Visible spectrum of aluminium oxide nanoparticles, the band was observed to be shifted towards the lower wavelength side ($\lambda_{max} = 237$ nm), which shows a blue shift (Fig. 3). This shift is attributed to regular arrangement of γ-Al_2O_3 particles which were considerably quantifiable in the synthesized samples (Ashraf et al., 2016), (Nguyen et al., 2017). Prashanth et al. (2015) obtained a similar absorption band and a corresponding energy band of 5.25eV for alumina nanoparticles.

Absorption positions depend on sizes and morphologies of the aluminium oxide nanoparticles. According to Khan et al. (2010) and Dobrzański et al. (2014), increase in the particle size or number of Al_2O_3 nanoparticles lead to an increase in their optical absorption. Ismail et al. (2017) also observed a decrease in the optical energy gap with increase in particle size and agglomeration of Al_2O_3 nanoparticles. Tilaki et al. (2007), observed a change in refractive index and consequently, the optical absorption of Al_2O_3 nanoparticles with their morphology,

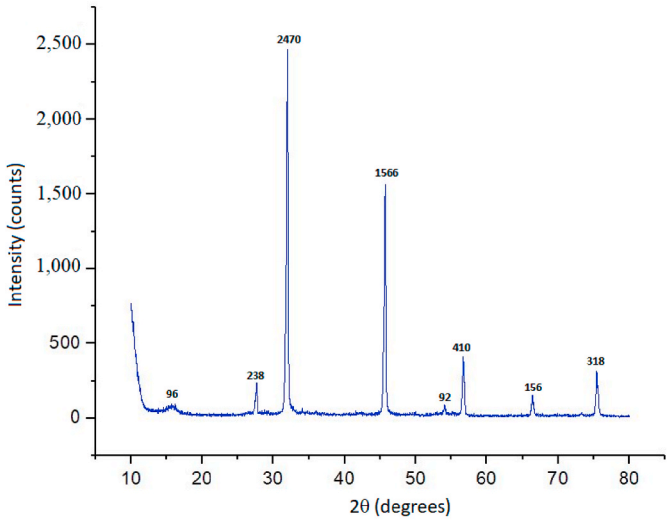

Fig. 2. X-ray diffractogram of the synthesized white aluminium oxide nanoparticles indicating the counts of the various peaks present.

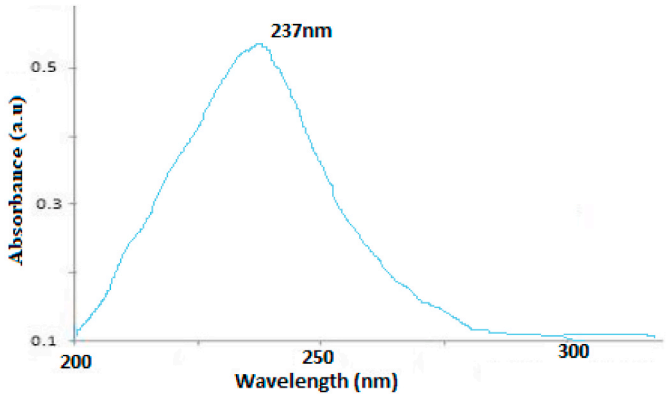

Fig. 3. UV spectra of white aluminium oxide nanoparticles.

topography and structure. In this regard, the UV-VIS absorption ability of aluminium oxide is related with band gap energy (≈5.25 eV) (Prashanth et al., 2015). A low band gap energy is desirable for easier conduction of electrons (high energy transitions) and thus faster transfer of electric charge.

3.3. Electrochemical performance of fabricated AIC

3.3.1. Open and closed-circuit voltage of fabricated AIC

The open circuit voltage (OCV[5]) of the fabricated AIC cells were significantly higher ($P > 0.05$) than the closed-circuit voltage (CCV[6]). The large deviation in potential is attributed to power loss (IR loss) resulting from resistance in the conductors used. The magnitude of both OCV and CCV produced in the cells was slightly lower than that of standard aluminium ion cells (2 V) (Lin et al., 2015). The deviation is attributed to the numerous changes in electrochemical environment subjected to the AIC one compared to the ideal one. It is however worthwhile noting that an OCV of 1.015 V for the AIC cells using standard Al_2O_3 and sulfuric acid electrolyte (electrode distance 1 cm) were observed. The corresponding OCV of its synthesized Al_2O_3 counterpart was significantly lower (833 mV) ($P < 0.05$). The deviation in potential values between the standard and synthesized aluminium ion cells are brought about by presence of impurities in the synthesized samples. Debris in the synthesized sample minimize the active electrode surface as well as interfere with the electrochemical environment present.

[5] Open current voltage.
[6] Closed current voltage.

Presence of debris affect the zeta potential of the electrode double layer (EDL,[7],[89]) by imparting foreign charges on the electrode-electrolyte film (Barany, 2015). These charges prevent conventional flow of current at the surface and therefore reduce the potential generated. Debris also react with the polymeric binders used to form bonds that affect the electrolytic environment at the EDL. FT-IR spectra (Fig. 1) confirmed presence of organic matter in the synthesized Al_2O_3. These compounds are known to form permanent covalent bonds with polymeric binders such as polyacrylate and silicone (Carlini et al., 2016), (Heinz et al., 2018) thus hindering current flow at the EDL. A suitable and cheap way to minimize presence of debris in synthesized Al_2O_3 particles (and electrode) is by use of rotary brushes. Acetone solution can be used to remove other non-polar contaminants such as oils prior to scrubbing. Scrubbing the surface of the synthesized electrode mechanically using rotary brushes is quite convenient with both thin and thick oxide layers. The brushes also remove any blurs on the surface of the electrodes. The deviation in both OCV and CCV values in the fabricated AIC cells was also quite significant ($P > 0.05$) as observed in Table 1.

The potential from sulfuric acid electrolyte was more than that from magnesium sulfate electrolyte. This is an anomaly to the conventional case whereby Mg^{2+} have a higher electrode reduction potential (-2.38v) compared to H^+ (0.00v) at standard electrochemical conditions. Both silicone and polyacrylate polymers have been confirmed to react with magnesium ions (Kihara et al., 2014), (Liechty et al., 2010). Reaction between the two form organometallic compounds that create an extra passivating film around the EDL thus interfere with flow of charges. The choice of electrode binder also influenced the resulting potential generated. For OCV, use of silicone binder significantly increased the OCV of the AIC ($P > 0.05$). There was no significance deviation in CCV resulting from use of silicone binder ($P < 0.05$) as illustrated in Table 1. The silane groups in silicone binder enhance more mechanical and thermal stability compared to polyacrylate adhesive (Magalhães et al., 2019) thus enabling a stable solution interphase during open circuit phenomenon. However, when the circuit is closed, the binder suffers from severe volume expansion during electrochemical cycling which affect the electrochemical environment. This leads to loss of current as illustrated in the CCV values.

3.3.2. Current-potential behavior of the fabricated AIC

All the electrochemical combinations of the AIC setups gave current-potential plots in the first quadrant of cartesian plane implying presence of passive components (loads) in the circuit. This is true since all the tests included a resistor in the circuit. The relation of the current-potential behavior was quite linear with a positive slope. The linearity of the relationship is an indicator of continuous drain voltage below their saturation points. From Fig. 4, the electrode combination of graphite and standard alumina with polyacrylate yielded the highest amount of cell current when using both electrolytes ($MgSO_4$ and H_2SO_4). The relatively higher cell capacities obtained while using polyacrylate were due to formation of stable solution interphase between polyacrylate binder and the two electrodes. Polyacrylic acid, the protonated version of polyacrylate is a common electrode binder with numerous lithium-ion (Li-ion) batteries (Wei et al., 2016), (Kasinathan et al., 2018). Polyacrylate metal complexes exhibit higher pore volumes (Zhang et al., 2012) thus increasing the net cell capacities. The saturation range in AIC while using standard Al_2O_3 with polyacrylate binder was longer for the sample in sulfuric acid electrolyte (560 mV) compared to magnesium sulfate electrolyte (355 mV). The drainage pattern in the latter was actually more exponential than linear citing presence of potential charge carrier microstates. The AIC setup using synthesized Al_2O_3 cathode and silicone binder gave the least cell capacity while using both sulfuric acid and magnesium sulfate electrolytes. The laggish electrochemical performance in this combination can be seen as arising from any debris in the electrode as well as poor passivation of silicone-electrolyte interface under charge-discharge stress. The electrochemical behavior of synthesized Al_2O_3 cathode using polyacrylate binder and standard Al_2O_3 cathode using silicone binder was close for both electrolytes. The two combinations also assumed a linear current-voltage behavior, citing high degree of ohmic behavior in their systems. The respective current-voltage behaviors of the different AIC combinations are illustrated in Fig. 4.

3.3.3. Current and power densities of the fabricated AIC

The current density values of the various AIC combinations ranged between 120.14A/cm^2 to 201.41A/cm^2. Increase in the electrode distance linearly decreased the current density. This is because the effective transport numbers of the charge carriers met more solution impedance as they travelled over a longer distance. More energy is also consumed in moving ions over a longer distance, effectively decreasing the current flux (Manthiram, 2017). The current and power density of the standard Al_2O_3 were significantly higher than those of the synthesized Al_2O_3 cathode combinations while using both binders and electrolytes ($P > 0.05$). This can be seen as a trickle-down effect from the corresponding CCV values. The obtained current density values were closely related to those of Kvande and Haupin (2000) who obtained similar values during modelling of aluminium electrolysis cells. The choice of electrolyte solution also impacted on the ultimate current and power densities. Sulfuric acid solution gave higher capacities in all the combinations of AIC tested. Magnesium ions readily combine with polyacrylate and silane groups in the electrode binders to give their corresponding organometallic complexes. These compounds decrease the net passivation of electrode-electrolyte film at the EDL thus hindering current movement. On the other hand, hydrogen ions from deprotonation of sulfuric acid react slowly with the two polymeric binders at ambient temperature environments. Usually, a catalyst (nickel, platinum or palladium) is required which was not so in this case. Therefore, most of the H^+ from sulfuric acid were readily ionizable in solution for current generation. The choice of binders used had a big impact on the current and power densities obtained. The current and power densities of polyacrylate binder combinations were significantly higher than those of the silicone binder combinations ($P > 0.05$) (Table 2). The highest power density was obtained in the graphite/standard Al_2O_3 electrode combination using sulfuric acid electrolyte and polyacrylate binder (137.97Watts/mm^2). The lowest power density value was 40.85Watts/mm^2 from graphite/synthesized Al_2O_3 electrode using magnesium sulfate electrolyte and silicone binder. The enhanced activity of polyacrylate binder combinations results from its mechanical, thermal and cell cycling stability during the working process of the cell (Zheng et al., 2017). These traits coupled with the excellent adhesion, cohesion and wetting properties of acrylate ions enable a conducive passivating film at the EDL thus more current and power densities. The average power density of the AIC with electrodes 1 cm apart was 97.665 $\pm$ 32.1335Watts/mm^2 (polyacrylate binder) and 80.11 $\pm$ 24.1857Watts/mm^2 (silicone binder) for all combinations. These magnitudes of power density are sufficient to power various small-scale gadgets without necessarily having to scale up the fabricated AIC potential. The current and power density values of the various fabricated AIC combinations are illustrated in Table 2.

3.3.4. Polarization of fabricated AIC electrodes and corrosion resistance

Polarization studies are crucial in determining the longevity of the electrodes (Tian et al., 2019), especially in presence of the two binders used versus their electrochemical efficiency. Polarization results from mechanical side-effects (of electrochemical process) that develop at the EDL interphase (Chen et al., 2018). The process is associated with overpotential, where a reverse electrochemical reaction takes place, reducing efficient cell performance and health (Armstrong and Hirst,

[7] Electrical double layer.
[8] Open and Closed-Circuit Voltages of the fabricated AIC.
[9] Current and power densities of the FAIC.

Table 1
Open and Closed-circuit voltage obtained from the fabricated AIC.

Electrode distance (cm) between Anode (graphite) and cathode	Open Circuit Voltage (mV)							
	Polyacrylate binder				Silicone binder			
	1M $MgSO_4$, 22.5 ± 1.5 °C		1M H_2SO_4, 22.5 ± 1.5 °C		1M $MgSO_4$, 22.5 ± 1.5 °C		1M H_2SO_4, 22.5 ± 1.5 °C	
	Cathode		Cathode		Cathode		Cathode	
	Std.Al_2O_3	Syn.Al_2O_3	Std.Al_2O_3	Syn.Al_2O_3	Std.Al_2O_3	Syn.Al_2O_3	Std.Al_2O_3	Syn.Al_2O_3
1	464	459	605	607	895	765	1015	833
3	453	444	591	590	887	741	1000	824
5	432	429	583	573	874	735	988	817
7	425	411	575	569	863	725	980	806
9	419	392	568	552	851	716	970	801
Closed Circuit Voltage (mV)								
1	439	415	570	541	414	405	540	529
3	420	402	560	526	401	389	528	518
5	411	385	540	512	388	376	515	504
7	399	371	519	501	377	359	509	489
9	379	366	499	486	368	340	488	477

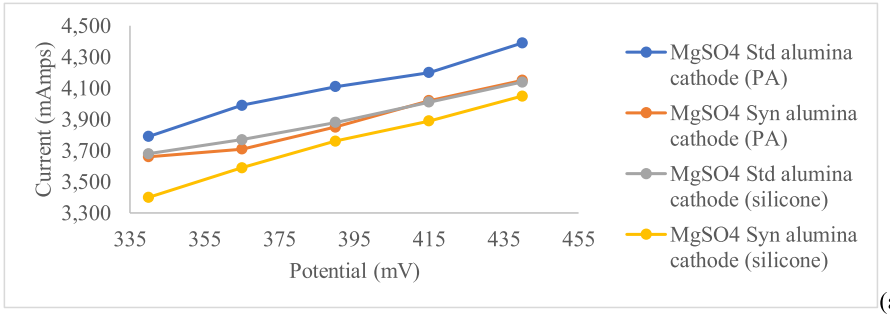

Fig. 4. Current-potential behavior of the various fabricated AIC combinations using magnesium sulfate electrolyte (a) and sulfuric acid electrolyte (b).

Table 2
The current and power density magnitudes obtained by various fabricated AIC combinations.

Electrode distance (cm) between Anode (graphite) and cathode	Current density (mA/mm^2)							
	Polyacrylate binder				Silicone binder			
	1M $MgSO_4$, 22.5 ± 1.5 °C		1M H_2SO_4, 22.5 ± 1.5 °C		1M $MgSO_4$, 22.5 ± 1.5 °C		1M H_2SO_4, 22.5 ± 1.5 °C	
	Cathode		Cathode		Cathode		Cathode	
	Std.Al_2O_3	Syn.Al_2O_3	Std.Al_2O_3	Syn.Al_2O_3	Std.Al_2O_3	Syn.Al_2O_3	Std.Al_2O_3	Syn.Al_2O_3
1	155.12	146.64	201.41	191.17	146.29	143.11	190.81	186.93
3	148.41	142.05	197.88	185.87	141.70	137.46	186.57	183.04
5	145.30	136.04	190.81	180.92	137.10	132.86	181.98	178.09
7	140.99	131.10	183.39	177.03	133.22	126.86	179.86	172.79
9	133.92	129.33	176.33	171.73	130.04	120.14	172.44	168.55
Power density (Watts/mm^2)								
1	88.42	60.86	137.97	103.42	60.56	57.96	103.04	98.88
3	83.11	57.10	132.58	97.77	56.82	53.47	98.51	94.81
5	78.46	52.38	124.22	92.63	53.20	49.96	93.72	89.76
7	73.17	48.64	116.09	88.69	50.22	45.54	91.55	84.50
9	66.83	47.33	108.80	83.46	47.85	40.85	84.15	80.40

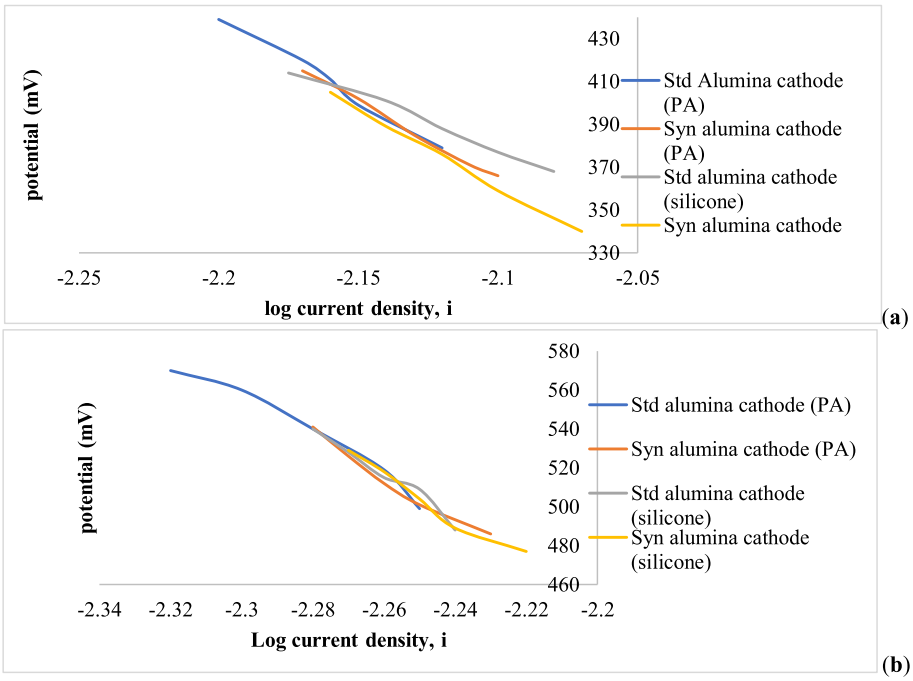

Fig. 5. The polarization curves of fabricated AIC combinations indicating the status of the electrodes in magnesium sulfate electrolyte (a) sulfuric acid electrolyte (b).

2011). The polarization curves obtained by the AIC combinations using sulfuric acid (Fig. 5b), gave a relatively more exponential appearance compared to those obtained using magnesium sulfate electrolyte (Fig. 5a). The exponential behavior of the AIC combinations in sulfuric acid indicate that the electrodes had surpassed the activation and Ohmic regions and were tending towards the trans-passive region (El-Bagoury et al., 2019), (Qin et al., 2019). This is an indicator that the electrodes exposed in sulfuric acid electrolyte had undergone several cycles and required replenishing of the electrolyte (concentration polarization). The standard Al_2O_3 cathode using polyacrylate binder had the most notable exponential curve. This is justified by the high current and power density obtained by its combinations. The AIC combinations of graphite/synthesized Al_2O_3 using silicone binder indicated the electrodes were still at the activation region (activation polarization). These electrodes had undergone fewer electrochemical cycles compared to the rest. This is also justified with their relatively lower current and power densities. AIC combinations of graphite/synthesized Al_2O_3 electrodes using silicone binder and graphite/standard Al_2O_3 using polyacrylate binder had similar polarization curves. The two were still in their Ohmic passivation stage and AIC efficiency here largely depended on the impedance of the cell. More time was thus required for the cells to undergo more electrochemical cycles and replenish. The polarization curves of the various fabricated AIC combinations are illustrated in Fig. 5.

The choice of binder affected status of the electrodes. The electrodes with polyacrylate binder were either in their Ohmic polarization region or concentration (trans-passive) polarization region. Therefore, these electrodes were likely to experience ion deposition or corrosion faster than those with silicone binders. Fast cycle time also affect the cell state-of-health (Barcellona et al., 2015), with the AIC combination of electrodes. The silicone binders were thus a good choice for preventing fast electrode corrosion.

4. Conclusions

Alumina nanoparticles were successfully synthesized and characterized from waste aluminium foils. The functional groups, crystallinity, particle size, phases and optical band gaps properties of these nanoparticles were characterized to resemble those of standard aluminium oxide nanoparticles. The nanoparticles were then used to fabricate aluminium ion cells, AICs which indicated great electrochemical potential. Their open and closed-circuit voltages, current-potential behavior, current and power densities as well as polarization curves were quite satisfactory for use as energy storage devices. This study indicates that waste aluminium foils can be converted to energy storage devices and in the process minimizing land pollution. The authors recommend optimization studies to be conducted on AICs fabricated using alumina nanoparticles.

Sources of funding

This research did not receive any specific grant from funding agencies in the public, commercial, or not-for-profit sectors.

Data availability statement

All the data used in the study is enclosed within the manuscript as well as any supplementary sheets attached.

Declaration of competing interest

The authors declare that they have no known competing financial interests or personal relationships that could have appeared to influence the work reported in this paper.

Acknowledgements

The authors are grateful to Maasai mara university, Chemistry lab and Vaal university of Technology, Analytical Chemistry lab for their assistance during the analysis of the synthesized nanoparticles. The authors wish to sincerely thank Mr. Rutto Kenneth, Mr. Lumumba Patrick and Md. Linda Mesoppirr (Maasai mara university) as well as (Mr. Evans Suter, Vaal university of technology) for facilitating these analyses.

References

Armstrong, F.A., Hirst, J., 2011. Reversibility and efficiency in electrocatalytic energy conversion and lessons from enzymes. Proc. Natl. Acad. Sci. U. S. A 108 (34), 14049–14054. https://doi.org/10.1073/pnas.1103697108.

Ashraf, J.M., Ansari, M.A., Khan, H.M., Alzohairy, M.A., Choi, I., 2016. Green synthesis of silver nanoparticles and characterization of their inhibitory effects on AGEs formation using biophysical techniques. Sci. Rep. 6, 20414. https://doi.org/10.1038/srep20414.

Ates, M., Demir, V., Arslan, Z., Daniels, J., Farah, I.O., Bogatu, C., 2015. Evaluation of alpha and gamma aluminum oxide nanoparticle accumulation, toxicity, and depuration in Artemia salina larvae. Environ. Toxicol. 30 (1), 109–118. https://doi.org/10.1002/tox.21917.

Badwal, S.P., Giddey, S.S., Munnings, C., Bhatt, A.I., Hollenkamp, A.F., 2014. Emerging electrochemical energy conversion and storage technologies. Frontiers in chemistry 2, 79. https://doi.org/10.3389/fchem.2014.00079.

Bagwell, R.B., Messing, G.L., Howell, P.R., 2001. The formation of α-Al_2O_3 from θ-Al_2O_3: the relevance of a "critical size" and: diffusional nucleation or "synchro-shear"? J. Mater. Sci. 36, 1833–1841. https://doi.org/10.1023/A:1017545213590, 2001.

Barany, S., 2015. Polymer adsorption and electrokinetic potential of dispersed particles in weak and strong electric fields. Adv. Colloid Interface Sci. 222, 58–69. https://doi.org/10.1016/j.cis.2014.09.009.

Barcellona, S., Brenna, M., Foiadelli, F., Longo, M., Piegari, L., 2015. Analysis of ageing effect on Li-polymer batteries. TheScientificWorldJOURNAL 979321. https://doi.org/10.1155/2015/979321, 2015.

Carlini, A.S., Adamiak, L., Gianneschi, N.C., 2016. Biosynthetic polymers as functional materials. Macromolecules 49 (12), 4379–4394. https://doi.org/10.1021/acs.macromol.6b00439.

Chen, Y., Huo, W., Lin, M., Zhao, L., 2018. Simulation of electrochemical behavior in Lithium ion battery during discharge process. PloS One 13 (1), e0189757. https://doi.org/10.1371/journal.pone.0189757.

Conroy, M., Soltis, J.A., Wittman, R.S., Smith, F.N., Chatterjee, S., Zhang, X., Ilton, E.S., Buck, E.C., 2017. Importance of interlayer H bonding structure to the stability of layered minerals. Sci. Rep. 7 (1), 13274. https://doi.org/10.1038/s41598-017-13452-7.

Djebaili, K., Mekhalif, Z., Boumaza, A., Djelloul, A., 2015. XPS, FTIR, EDX, and XRD analysis of Al_2O_3 scales grown on PM2000 alloy. Journal of spectroscopy 15, 16. https://doi.org/10.1155/2015/868109.

Dobrzański, L.A., Szindler, M., Drygała, A., et al., 2014. Silicon solar cells with Al2O3 antireflection coating. centr.eur.j.phys. 12, 666–670. https://doi.org/10.2478/s11534-014-0500-9.

El-Bagoury, N., Ahmed, S.I., Ahmed Abu Ali, O., El-Hadad, S., Fallatah, A.M., Mersal, G., Ibrahim, M.M., Wysocka, J., Ryl, J., Boukherroub, R., A Amin, M., 2019. The influence of microstructure on the passive layer Chemistry and corrosion resistance for some titanium-based alloys. Materials 12 (8), 1233. https://doi.org/10.3390/ma12081233.

Heinz, D., Amado, E., Kressler, J., 2018. Polyphilicity-an extension of the concept of amphiphilicity in polymers. Polymers 10 (9), 960. https://doi.org/10.3390/polym10090960.

Hoshyar, N., Gray, S., Han, H., Bao, G., 2016. The effect of nanoparticle size on in vivo pharmacokinetics and cellular interaction. Nanomedicine 11 (6), 673–692. https://doi.org/10.2217/nnm.16.5.

Iijima, S., Yumura, T., Liu, Z., 2016. One-dimensional nanowires of pseudoboehmite (aluminum oxyhydroxide γ-AlOOH). Proc. Natl. Acad. Sci. U. S. A 113 (42), 11759–11764. https://doi.org/10.1073/pnas.1614059113.

Ismail, R.A., Zaidan, S.A., Kadhim, R.M., 2017. Preparation and characterization of aluminum oxide nanoparticles by laser ablation in liquid as passivating and anti-reflection coating for silicon photodiodes. Appl. Nanosci. 7, 477–487. https://doi.org/10.1007/s13204-017-0580-0.

Kasinathan, R., Marinaro, M., Axmann, P., Wohlfahrt-Mehrens, M., 2018. Influence of the molecular weight of poly-acrylic acid binder on performance of Si-Alloy/Graphite composite anodes for lithium-ion batteries. Energy Technol. 6 (11), 2256–2263. https://doi.org/10.1002/ente.201800302.

Khan, S.Z., Liu, Z., Li, L., 2010. Characteristics of γ-Al2O3 nanoparticles generated by continuous-wave laser ablation in liquid. Appl. Phys. A 101, 781–787. https://doi.org/10.1007/s00339-010-5936-1, 2010.

Kihara, Y., Ichikawa, T., Abe, S., 2014. Synthesis of alkyne-functionalized amphiphilic polysiloxane polymers and formation of nanoemulsions conjugated with bioactive molecules by click reactions. Polym. J. 46, 175–183. https://doi.org/10.1038/pj.2013.86, 2014.

Klotz, K., Weistenhöfer, W., Neff, F., Hartwig, A., van Thriel, C., Drexler, H., 2017. The health effects of aluminum exposure. Deutsches Arzteblatt international 114 (39), 653–659. https://doi.org/10.3238/arztebl.2017.0653.

Krewski, D., Yokel, R.A., Nieboer, E., Borchelt, D., Cohen, J., Harry, J., Kacew, S., Lindsay, J., Mahfouz, A.M., Rondeau, V., 2007. Human health risk assessment for aluminium, aluminium oxide, and aluminium hydroxide. J. Toxicol. Environ. Health B Crit. Rev. 10 (Suppl. 1), 1–269. https://doi.org/10.1080/10937400701597766. Suppl 1.

Kvande, H., Haupin, W., 2000. Cell voltage in aluminum electrolysis: a practical approach. J. Occup. Med.: J. Miner. Met. Mater. Soc. 52 (2), 31–37. https://doi.org/10.1007/s11837-000-0044-x.

Leustek, T., 2002. Sulfate metabolism. Arabidopsis Book 1, e0017. https://doi.org/10.1199/tab.0017.

Li, C., McLinden, C., Fioletov, V., Krotkov, N., Carn, S., Joiner, J., Streets, D., He, H., Ren, X., Li, Z., Dickerson, R.R., 2017. India is overtaking China as the world's largest emitter of anthropogenic sulfur dioxide. Sci. Rep. 7 (1), 14304. https://doi.org/10.1038/s41598-017-14639-8.

Liechty, W.B., Kryscio, D.R., Slaughter, B.V., Peppas, N.A., 2010. Polymers for drug delivery systems. Annual review of chemical and biomolecular engineering 1, 149–173. https://doi.org/10.1146/annurev-chembioeng-073009-100847.

Lin, M.C., Gong, M., Lu, B., Wu, Y., Wang, D.Y., Guan, M., Angell, M., Chen, C., Yang, J., Hwang, B.J., Dai, H., 2015. An ultrafast rechargeable aluminium-ion battery. Nature 520 (7547), 325–328. https://doi.org/10.1038/nature14340.

Magalhães, S., Alves, L., Medronho, B., Fonseca, A.C., Romano, A., Coelho, J., Norgren, M., 2019. Brief overview on bio-based adhesives and sealants. Polymers 11 (10), 1685. https://doi.org/10.3390/polym11101685.

Mahmood, N., Hou, Y., 2014. Electrode nanostructures in lithium-based batteries. Advanced science (Weinheim, Baden-Wurttemberg, Germany) 1 (1), 1400012. https://doi.org/10.1002/advs.201400012.

Manthiram, A., 2017. An outlook on lithium ion battery technology. ACS Cent. Sci. 3 (10), 1063–1069. https://doi.org/10.1021/acscentsci.7b00288.

Mikhaylo, A.T., Mirko, S., Xiaoying, Z., Edward, L.D., 2005. Effect of polymorphic phase transformations in Al_2O_3 film on oxidation kinetics of aluminum powders. Combust. Flame 140 (4), 310–318. https://doi.org/10.1016/j.combustflame.2004.10.010.

Nguyen, D.K., Lee, H., Kim, I.T., 2017. Synthesis and thermochromic properties of Cr-doped Al_2O_3 for a reversible thermochromic sensor. Materials 10 (5), 476. https://doi.org/10.3390/ma10050476.

Oh, D., Qi, J., Lu, Y.C., Zhang, Y., Shao-Horn, Y., Belcher, A.M., 2013. Biologically enhanced cathode design for improved capacity and cycle life for lithium-oxygen batteries. Nat. Commun. 4, 2756. https://doi.org/10.1038/ncomms3756.

Prasad, S., Mandal, I., Singh, S., Paul, A., Venkatramani, R., Swaminathan, R., 2017. Near UV-Visible electronic absorption originating from charged amino acids in a monomeric protein. Chem. Sci. 8 (8), 5416–5433. https://doi.org/10.1039/c7sc00880e.

Prashantha, P.A., Raveendraa, R.S., Hari, K., Ananda, S., Baghya, N.P., Nagabhushana, B. M., Lingaraju, H., Raja, N., 2015. Synthesis, characterizations, antibacterial and photoluminescence studies of solution combustion-derived α-Al_2O_3 nanoparticles. Journal of Asian Ceramic Societies 3 (3), 345–351. https://doi.org/10.1016/j.jascer.2015.07.001.

Qin, R., Du, Y., Xu, Z., Lu, M., 2019. Anodic polarization behavior of X80 steel in Na_2SO_4 solution under high potential and current density conditions. Materials 12 (3), 394. https://doi.org/10.3390/ma12030394.

Roselin, L.S., Juang, R.S., Hsieh, C.T., Sagadevan, S., Umar, A., Selvin, R., Hegazy, H.H., 2019. Recent advances and perspectives of carbon-based nanostructures as anode materials for Li-ion batteries. Materials 12 (8), 1229. https://doi.org/10.3390/ma12081229.

Santos, P., Coelho, A.C.V., Santos, H., Kiyohara, P.K., 2009. Hydrothermal synthesis of well-crystallised boehmite crystals of various shapes. Mater. Res. 12 (4), 437–445. https://doi.org/10.1590/S1516-14392009000400012.

Tian, R., Park, S., King, P.J., 2019. Quantifying the factors limiting rate performance in battery electrodes. Nat. Commun. 10, 1933. https://doi.org/10.1038/s41467-019-09792-9.

Tilaki, R., Iraji zad, A., Mahdavi, S., 2007. Size, composition and optical properties of copper nanoparticles prepared by laser ablation in liquids. Appl. Phys. A 88, 415–419. https://doi.org/10.1007/s00339-007-4000-2.

Toigo, C., Arbizzani, C., Pettinger, K.H., Biso, M., 2020. Study on different water-based binders for Li4Ti5O12 electrodes. Molecules 25 (10), 2443. https://doi.org/10.3390/molecules25102443.

Umemoto, K., Wentzcovitch, R.M., 2008. Prediction of an U2S3-type polymorph of Al_2O_3 at 3.7 mbar. Proc. Natl. Acad. Sci. U. S. A 105 (18), 6526–6530. https://doi.org/10.1073/pnas.0711925105.

Vailionis, A., Gamaly, E.G., Mizeikis, V., Yang, W., Rode, A.V., Juodkazis, S., 2011. Evidence of superdense aluminium synthesized by ultrafast microexplosion. Nat. Commun. 2, 445. https://doi.org/10.1038/ncomms1449.

Wang, Z.Y., Zhang, R.J., Lu, H.L., Chen, X., Sun, Y., Zhang, Y., Wei, Y.F., Xu, J.P., Wang, S.Y., Zheng, Y.X., Chen, L.Y., 2015. The impact of thickness and thermal annealing on refractive index for aluminum oxide thin films deposited by atomic layer deposition. Nanoscale research letters 10, 46. https://doi.org/10.1186/s11671-015-0757-y.

Wang, X., Peng, X., Tan, X., 2016. The reactive element effect of ceria particle dispersion on alumina growth: a model based on microstructural observations. Sci. Rep. 6, 29593. https://doi.org/10.1038/srep29593, 2016.

Wang, F., Fan, X., Gao, T., Sun, W., Ma, Z., Yang, C., Han, F., Xu, K., Wang, C., 2017. High-voltage aqueous magnesium ion batteries. ACS Cent. Sci. 3 (10), 1121–1128. https://doi.org/10.1021/acscentsci.7b00361.

Wei, L., Chen, C., Hou, Z., Wei, H., 2016. Poly (acrylic acid sodium) grafted carboxymethyl cellulose as a high performance polymer binder for silicon anode in lithium ion batteries. Sci. Rep. 6, 19583. https://doi.org/10.1038/srep19583.

Yin, Z., Tordjman, M., Lee, Y., Vardi, A., Kalish, R., Del Alamo, J.A., 2018. Enhanced transport in transistor by tuning transition-metal oxide electronic states interfaced with diamond. Science advances 4 (9), eaau0480. https://doi.org/10.1126/sciadv.aau0480.

Yusuf, N.K., Lajis, M.A., Ahmad, A., 2019. Multiresponse optimization and environmental analysis in direct recycling hot press forging of aluminum AA6061. Materials 12 (12), 1918. https://doi.org/10.3390/ma12121918.

Zhang, Y.B., Zhou, H.L., Lin, R.B., Zhang, C., Lin, J.B., Zhang, J.P., Chen, X.M., 2012. Geometry analysis and systematic synthesis of highly porous isoreticular frameworks with a unique topology. Nat. Commun. 3, 642. https://doi.org/10.1038/ncomms1654.

Zheng, T., Jia, Z., Lin, N., Langer, T., Lux, S., Lund, I., Gentschev, A.C., Qiao, J., Liu, G., 2017. Molecular spring enabled high-performance anode for lithium ion batteries. Polymers 9 (12), 657. https://doi.org/10.3390/polym9120657.